Relationships between Electrification and Storm-Scale Properties Based on Idealized Simulations of an Intensifying Hurricane-Like Vortex

ALEXANDRE O. FIERRO

Cooperative Institute for Mesoscale Meteorological Studies, University of Oklahoma, and NOAA/OAR/National Severe Storms Laboratory, Norman, Oklahoma

EDWARD R. MANSELL

NOAA/OAR/National Severe Storms Laboratory, Norman, Oklahoma

(Manuscript received 7 July 2017, in final form 7 November 2017)

ABSTRACT

This study investigates relationships between storm-scale properties and the electrification and lightning of two simulations of an intensifying idealized tropical cyclone (TC) using the cloud-resolving Collaborative Model for Multiscale Atmospheric Simulation (COMMAS). To produce an intensifying storm, an initial weak TC is subjected to a linear increase in sea surface temperature.

As the TC intensifies, lightning flash rates increase in both the inner core ($r \leq 100$ km) and outer region ($100 < r \leq 300$ km). As time progresses, lightning in the outer region gradually decreases, while the inner-core lightning remains relatively steady. Bootstrapped correlation statistics using 1000 random samples between the pressure trace and time series of lightning rates shows a statistically significant negative correlation between inner-core lightning and TC intensification. Lightning rates in the outer bands were found to lag minimum surface pressure by 12 h.

The increases in lightning in both the inner core and outer region coincided well with increases in 0.5 g kg^{-1} graupel and 5 m s^{-1} updraft volumes in each respective region. Correlation statistics with selected kinematic and microphysical variables known to be associated with lightning in thunderstorms, such as the ice water path, integrated updraft volume, and graupel volume, revealed that their increase in the inner core indicated an ongoing deepening, similar to the lightning. Trends in these proxy variables in the outer bands were also found to lag TC intensification by 12 h.

Overall, the best linear relationships with lightning in either the inner core or the outer region were obtained with the 0.5 g kg^{-1} graupel volume and total graupel mass.

1. Introduction

Given the well-established relationship between convective cloud processes in the inner core of tropical cyclones (TCs) and their intensity (e.g., Anthes 2003; Hendricks et al. 2004; Montgomery et al. 2006; Nolan et al. 2007; Guimond et al. 2010; Fierro and Reisner 2011; Rogers et al. 2013, 2016), trends in cloud-to-ground (CG) lightning activity within TCs have also been found to exhibit some association with storm intensity changes (e.g., Lyons et al. 1989; Molinari et al. 1994, 1999; Kelley et al. 2004; Samsury and Orville 1994; Shao et al. 2005; Squires and Businger 2008; Price et al. 2009; Fierro et al. 2011; Bovalo et al. 2014; Stevenson et al. 2016). Most of these studies reported that bursts of inner-core lightning (mostly CG flashes) were a potential precursor to storm intensification. This relationship did not hold across all TC cases investigated because the future intensity trend of the TC was often contingent upon the prior trend, with changes in trend (weakening to intensifying or vice versa) being more likely within 6–12 h following an inner-core burst (e.g., Molinari et al. 1999). A handful of recent observational studies have further suggested that, regardless of the previous intensity trend, inner-core lightning bursts coincided with the end of an intensification phase or with the weakening of the TC (Thomas et al. 2010; DeMaria et al. 2012). These studies also found that lightning in the outer bands of the TC was a preferred surrogate

Corresponding author: Alexandre O. Fierro, alex.fierro@noaa.gov

DOI: 10.1175/JAS-D-17-0202.1

for the imminent intensification of the TC. Besides understanding the processes connecting lightning and TC intensity (or intensity changes), there is wide interest in applications of lightning observations to diagnose or forecast TC characteristics.

Relatively few modeling endeavors have included explicitly simulated cloud-scale electrification processes within TCs: namely, Fierro et al. (2007), Fierro and Reisner (2011), Fierro et al. (2013, 2015), and Fierro and Mansell (2017, hereafter FM17). Using idealized TC simulations, FM17 investigated some of the relationships between electrification/lightning, storm intensity, and various cloud-scale properties of the TC. Their study placed emphasis on a steady-state strong TC and two weakening TC scenarios. For the steady-state case, electrical activity in either the inner core (radius $r \leq 100$ km) or the outer region ($100 < r \leq 300$ km) exhibited noteworthy linkages with cloud-scale properties that were similar to those documented in electrified convective storms (e.g., MacGorman et al. 1989; MacGorman and Rust 1998; Lang and Rutledge 2002; Wiens et al. 2005; Mansell et al. 2005; Fierro et al. 2006; Kuhlman et al. 2006). For instance, total lightning trends were generally well associated with trends in updraft volume and graupel volume. Despite a nearly identical filling rate, the two weakening cases exhibited a contrasting relationship between pressure rise and inner-core lightning rate: the first weakening TC case (SST) had a gradually reduced homogeneous sea surface temperature, and the second case (SHEAR) introduced deep shear into the base state. The inner-core lightning of the SST case decreased monotonically, whereas the SHEAR case produced a marked increase in inner-core lightning before the TC eventually became torn apart.

The present study is a logical follow-on to FM17 by conducting a parallel analysis for the case of an intensifying TC. Emphasis on this is pertinent to the challenge of accurate prediction of intensification cycles of TCs given their greater potential for loss of life and property (e.g., Pielke and Landsea 1998; Schmidt et al. 2009). Comparatively few modeling studies thus far focused on the relationships between explicitly simulated electrification and selected key microphysical and dynamical variables within TCs (let alone intensifying ones), thus a thorough analysis of the mechanism(s) at play during the intensification of the TCs in the present simulations is beyond the scope of this study.

2. Numerical model and experimental design

This work employs the Collaborative Model for Multiscale Atmospheric Simulation (COMMAS; Wicker and Wilhelmson 1995; Coniglio et al. 2006), which is based on the equation set of Klemp and Wilhelmson (1978). The cloud microphysics are modeled by the NSSL two-moment, four-ice-category bulk scheme (Mansell et al. 2010; Ziegler 1985; Mansell and Ziegler 2013). Noninductive charging parameterizations were derived from Saunders and Peck (1998) and Brooks et al. (1997) and inductive charging from Ziegler et al. (1991). The electric field is computed from the charge distribution using an elliptic equation solver (Dendy 1987; Dendy and Moulton 2010), and lightning discharges are simulated by the three-dimensional stochastic branched lightning scheme of Mansell et al. (2002). The horizontal grid is the same as FM17, namely, a 450×450 point, 1600×1600 km^2 domain with constant 2.5-km spacing on an inner-grid area of 600×600 km^2 and stretched to 5 km in the outer-grid region. The horizontal spacing for the lightning computation is half that of the regular grid (i.e., 1.25 km stretched to 2.5 km).

The vertical grid has 60 levels with a grid spacing stretching from 100 m at the lowest level to a maximum of 500 m above 8.25 km MSL. The model top is set at 22 km MSL. The equations of motion were integrated on an f plane with a constant assumed latitude of 25° and an initial background flow at rest. The time step was set to 5 s with open lateral boundary conditions. A Newtonian cooling term was applied in the simulations following Rotunno and Emanuel (1987) to help reduce the detrimental effects of subsidence in the far field after long integrations. For more details behind the numerical model, parameterizations used, initialization procedures, and settings of the simulation domain, the reader is invited to consult FM17.

In this work, two separate simulations of an intensifying TC were conducted. This was achieved by restarting from a selected time the SST simulation presented in FM17, which produced a weakening TC. Recall that for their SST experiment, the horizontally homogeneous SST was linearly decreased over the first 10 h of simulation (out of a total of 30 h) from an initial value of 27°C down to 22°C. To produce an intensifying TC, the output from the SST simulation at 34 h was used as initial conditions of a new simulation wherein the SST was subsequently increased from its initial low value of 22°C to a value above 26°C (e.g., Williams and Renno 1993). To balance the high computational burden of these simulations with the desire to obtain a larger sample size (i.e., broader range of lightning rates), two separate simulations were devised: the first increased the SST to 28°C (SST28), and the second to 30°C (SST30). This gradual SST increase was applied over the first 7 h with each simulation integrated for a total of 36 h. COMMAS does not include an ocean model (surface conditions are thus specified) and does not include a full radiation scheme.

3. Results

For consistency and to facilitate comparison, the analysis focuses on the same two TC regions on a storm-centered cylindrical grid defined in FM17, namely, the inner core ($r \leq 100$ km) and the outer region ($100 < r \leq 300$ km). It is relevant to reiterate that this particular definition of the outer region includes both the outer-rainband region and part of the inner-band region characterized, respectively, by the maximum and a minimum in lightning within the TC (Cecil et al. 2002; Cecil and Zipser 2002). As in FM17, all height levels are above mean sea level (MSL).

a. General evolution

Both simulations produced qualitatively similar evolution in terms of intensity trend [as measured by the minimum surface pressure (minSLP)] and lightning trends in both the inner core and outer region (Fig. 1). A few hours after the onset of pressure fall, both the inner core and outer region exhibited a marked increase in lightning rates. For SST28, which, as anticipated, produced a less intense storm than SST30 (minSLP of 935 hPa compared to 910 hPa), the onset of the intensification period occurred about 5 h later than in SST30. Concomitant with this, noticeable growth in storm-total lightning activity occurred later in SST28 than in SST30, namely, ~9–10 h into the simulation for SST30 compared to about 18 h for SST28 (Figs. 1a,b). The lightning activity in the outer region gradually faded in both simulations after the first 8–10 h of higher flash rates (Fig. 1). Given that lightning detected within observed TCs (i) primarily consists of CG flashes, (ii) is episodic, and (iii) varies noticeably from case to case, the simulated total flash rates in FM17 and, by extension, those in Fig. 1 herein are within the range of observed values (e.g., Molinari et al. 1999; DeMaria et al. 2012) when scaled by an average intracloud:CG ratio of roughly 3:1 for nonsevere storms (Boccippio et al. 2001; Schultz et al. 2011).

Our examination of how lightning behaviors relate to particular changes in basic storm structures begins with an inspection of the evolution of the spatial collocation of the horizontal precipitation structure and the respective locations of lightning-active regions in the horizontal (Fig. 2) and in the Hovmöller space (Fig. 3). Note that because the SST is gradually increased from an initial value of 22°C to a final target value above 26°C over a 7-h period, the vortex continues to spin down during the first 5–7 h in both simulations (Fig. 3) because the SST is still relatively cool. The TC in both simulations then begins intensifying once the SST reaches about 26°C (Williams and Renno 1993). Before organizing into a well-defined eyewall (Figs. 2c,d,g), convective precipitation regions

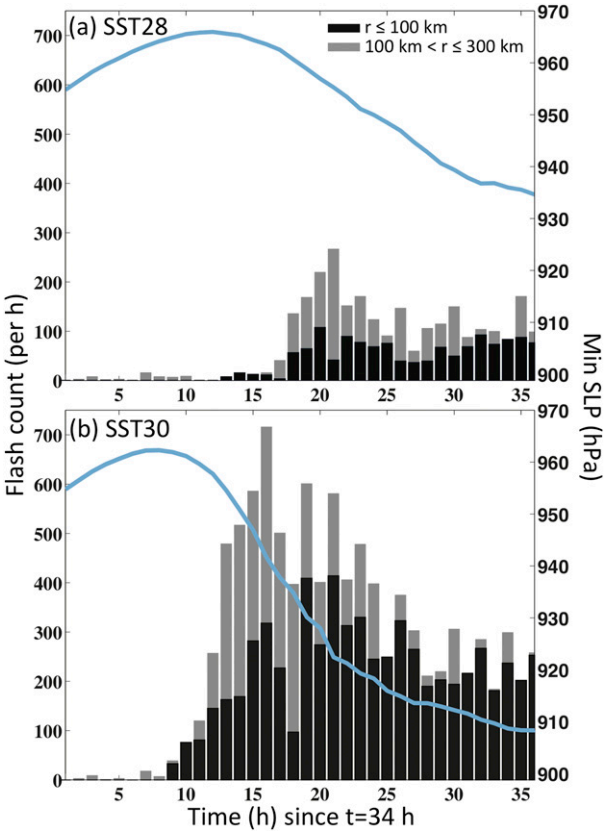

FIG. 1. Stacked bar charts of the time series of the hourly flash rates for (a) SST28 and (b) SST30 on the native Cartesian grid. The flash rates were computed on prescribed storm-centered cylinders containing the outer region (gray portion of each bar) and inner-core region (black portion of each bar). The inner-core rates include all flashes within a radius $r = 100$ km from the storm center, and the rates of the outer region include all flashes within $100 < r \leq 300$ km. The storm center is the gridpoint location with the minimum total pressure at the surface. The sum of the respective flash rates of the black and gray portions of each bar represents the "storm total" rate, which is shown on the left y axis (i.e., over the entire $r = 300$-km storm-centered cylinder mask). The time series also show the surface pressure trace (hPa) for each experiment as a solid black line (right y axis). To facilitate comparison, the respective scale for the storm-total flash rates and the pressure trace use the same upper and lower bounds for each experiment.

(dBZ > 40 at 1 km) in both simulations gradually increase in area in the periphery ($r \sim 60$–100 km) of an initial center of circulation predominantly characterized by weak to moderate precipitation (dBZ ≤ 40; Figs. 2a, 3) and weak updrafts ($W < 5\ \mathrm{m\ s^{-1}}$; Fig. 4g). The earlier and sharper pressure fall in SST30 is manifested by a more rapid organization of deep moist convection around the inner core, as evidenced by heightened lightning activity there in comparison to SST28 (Figs. 2b–g).

Successive snapshots of storm-centered radius–height diagrams of the radial winds (Vr) and tangential winds (Vt; Figs. 4a–f) alongside a Hovmöller diagram of mean

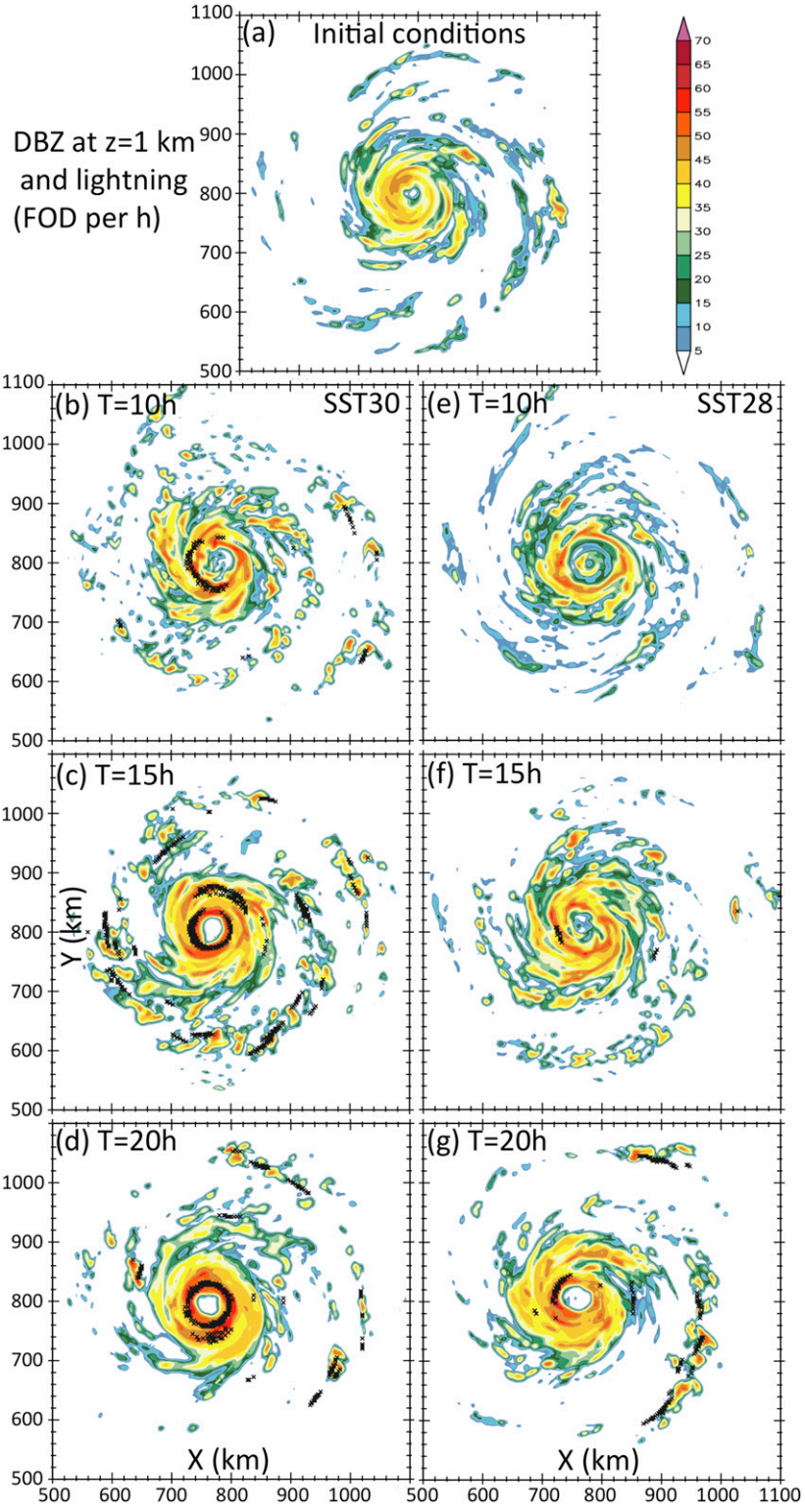

FIG. 2. Horizontal cross sections of radar reflectivity fields at 1 km MSL overlaid with the hourly lightning initiation locations (black cross) for (b)–(d) SST30 and (e)–(g) SST28 during intensification at 10, 15, and 20 h, respectively. (a) The initial conditions, which are identical for both simulations, are shown for reference.

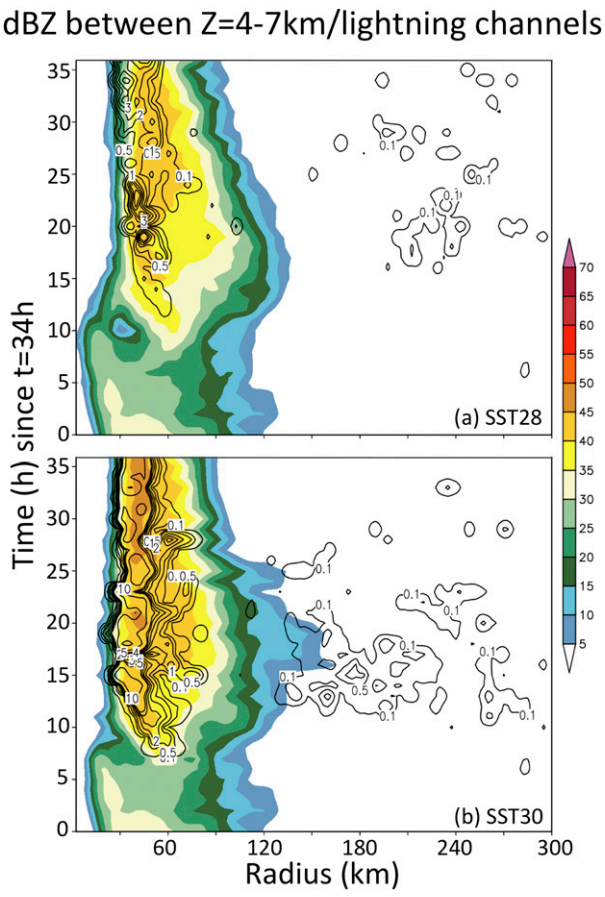

FIG. 3. Storm-centered Hovmöller diagrams of the radar reflectivity fields averaged within the layer 4–7 km MSL and overlaid with the azimuthally averaged total number of lightning channels (sum of positive and negative channels; black contours) for (a) SST28 and (b) SST30.

midlevel vertical velocities (Fig. 4g) illustrate the gradual enhancement of the secondary circulation of the TC in SST30 during intensification (SST28 being qualitatively similar). The intensification of the vortex involved the merging of moderate updrafts ($W \geq 5\,\mathrm{m\,s^{-1}}$ above 5 km AGL) collocated with appreciable vertical vorticity ($\zeta \geq 10^{-4}\,\mathrm{s^{-1}}$; not shown) near $r = 60$ km (Fig. 4g) into a well-defined ring (e.g., Hendricks et al. 2004; Montgomery et al. 2006). At ~7–8 h, axisymmetric midlevel updraft speeds on the order of 2–3 $\mathrm{m\,s^{-1}}$ appear near $r = 60$ km and progressively move inward near $r = 40$ km as time progresses (Fig. 4g). This is indicative of the simultaneous contraction and axisymmetrization of the eyewall convection. This behavior is also seen in SST28 a few (i.e., 2–3) hours later, as evidenced by the appearance of a distinct outer eyewall at 10 h (Fig. 2e). During the intensification period, deep moist convection in the eyewall is usually located around the radius of maximum tangential winds, with some convection occurring inside it (Figs. 4d–g). This behavior is consistent with many recent modeling studies suggesting a noteworthy association between TC intensification and the presence of deep moist convection near and, particularly, inside the radius of maximum winds where latent heating can be more efficiently retained in the inner core (e.g., Nolan et al. 2007; Rogers et al. 2013, 2016; Guimond et al. 2010, 2016; Hazelton et al. 2017).

The organization of convective updrafts around the inner core is reflected by a simultaneous increase in inner-core lightning (Fig. 4g). Consistent with many modeling studies, the strengthening of the radial inflow within the lowest kilometer is coincident with an increase in outflow between 1 and 2 km (associated with a persistent updraft component) just inside the radius of maximum tangential winds [$r \sim 15$–30 km; cf. Figs. 4c,e; Smith and Montgomery (2015) and citations therein]. This localized strong outflow region just above the boundary layer was shown to arise from a departure from gradient wind balance near the top of the boundary layer (i.e., supergradient flow; Smith and Montgomery 2015).

As each TC gradually intensifies, the radial width of the eyewall reflectivity slightly contracts (Fig. 3) while the lightning activity in the outer region gradually wanes (Figs. 1 and 3). This reduction in lightning in the outer region is associated with a gradual weakening of the convection in the far field, which is a well-documented, longstanding limitation of long integrations of idealized TC simulations (e.g., Rotunno and Emanuel 1987; D. Nolan 2016, personal communications; FM17). This is discussed in more detail in the conclusions.

To provide a more comprehensive view of the relationships between the electrification in both regions of the TC and their bulk microphysical and kinematic quantities, time–height volume plots of total lightning channels (>0.5), graupel mass (>0.5 $\mathrm{g\,kg^{-1}}$), and vertical velocities (>5 $\mathrm{m\,s^{-1}}$) were computed (Fig. 5). These also provide further evidence that, as time progresses, the inner-core updrafts (and, hence, secondary circulation) and graupel volume increase coincidentally with the weakening of the convection in the outer region. As also seen in Fig. 1, this development is more pronounced for SST30. One interesting behavior can be noted in both simulations for the inner-core volumes: after the period of largest pressure drop (at about 20–22 h), the highest altitudes of the lower-value contours of graupel, updraft speeds, and, hence, lightning channels also exhibit a gradual descent with time (Fig. 5). This descent of the maximum altitudes of hydrometeors (Figs. 5b,e) and, hence, charge volumes (not shown) in the inner core is coincident with an increase of intracloud (IC) flashes in both simulations at lower levels (<7 km; not shown). Akin to the strengthening convection in the

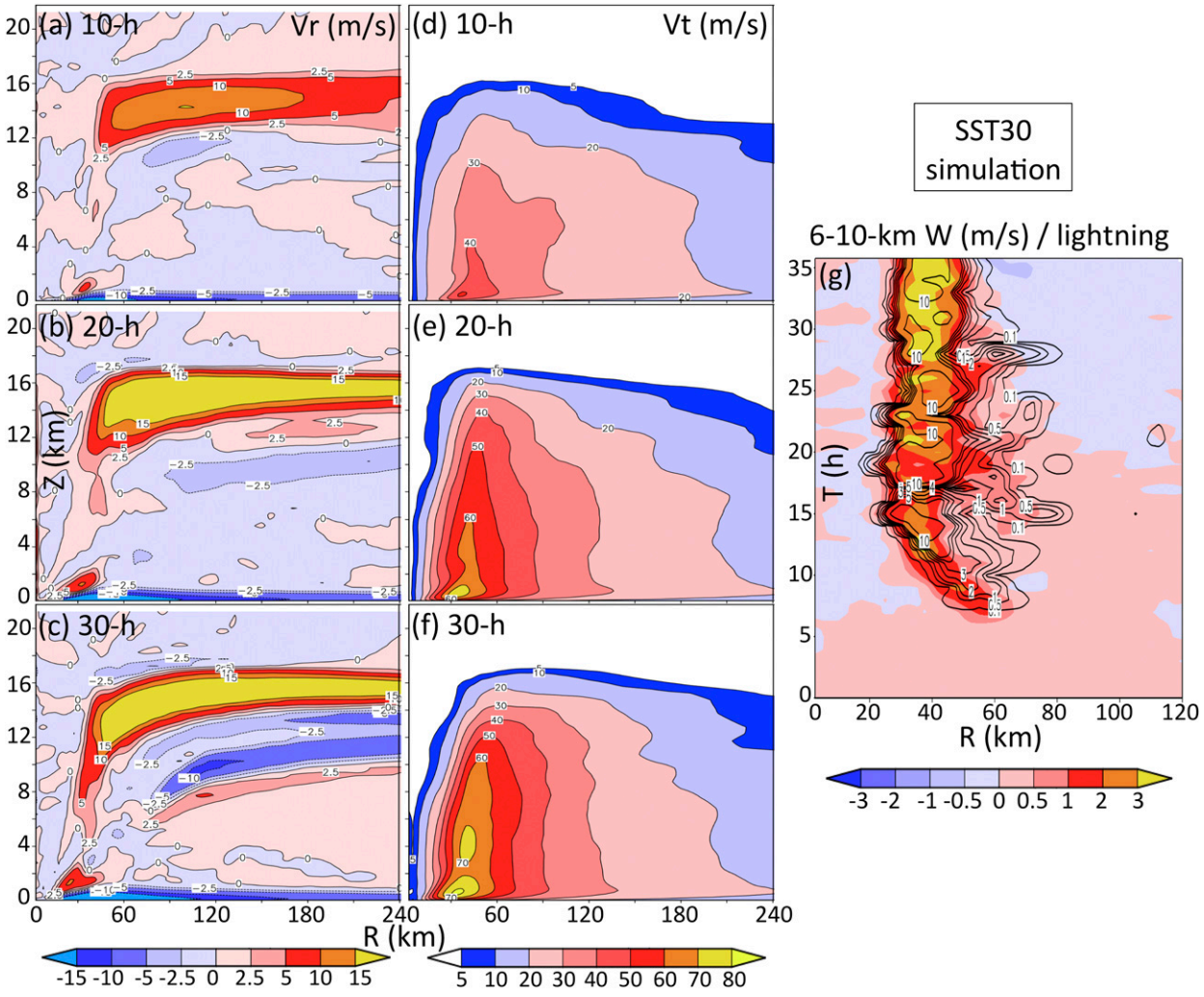

FIG. 4. Radius–height diagrams of radial winds (Vr; m s^{-1}) at (a) 10, (b) 20, and (c) 30 h of simulation. (d)–(f) As in (a)–(c), respectively, but for the tangential winds (Vt; m s^{-1}). (g) Storm-centered Hovmöller diagram of layer-averaged 6–10-km vertical velocities (shaded contours) overlaid with total lightning channels (black contours). The legends for colors and shading are shown at the bottom of each corresponding column. The results in this figure are for SST30.

inner core of the control case in FM17, the increase in low-level (<7 km) ICs in both runs is associated with the formation and progressive enhancement of a main negative charge region at midlevels (~7–9 km) atop a layer of positive charge as indicated by regions of space charge density magnitudes exceeding 0.1 nC m^{-3} in the inner core (Fig. 6c). Contours of lower space charge magnitude threshold (not shown) reveal a persistent weaker upper (>9 km) positive charge region. Consequently, the gross charge structure in the eyewall convection could be classified as a bottom-heavy normal tripole (Mansell et al. 2010). This strengthening of the main midlevel charge region in the inner core arises from an increase in magnitude (and volume; not shown) of noninductive negative charging between graupel and ice crystals/snow (7–9 km in Fig. 6a), which is associated with an increase in graupel volume (Figs. 5b,e) and mass (Figs. 6a,c). At lower levels in the inner core, graupel acquires positive charge, owing to higher ambient temperatures and sufficient cloud water contents (CWCs; below 7 km in Figs. 6a,c). In terms of net charge magnitude and volumetric extent, the dominant lower-level dipole of the bottom-heavy tripole (Fig. 6c) is associated with equally strong magnitudes of negative and positive electrical potential (not shown). As shown in Mansell et al. (2010), such a vertical configuration of electrical potential would favor the production of lower-level IC flashes (near and below 7 km; Fig. 6c). Because the magnitude of the lower positive electrical potential is comparable to the midlevel negative potential (not shown), the downward-propagating negative leaders of IC discharges initiating at ~7 km will carry a weak

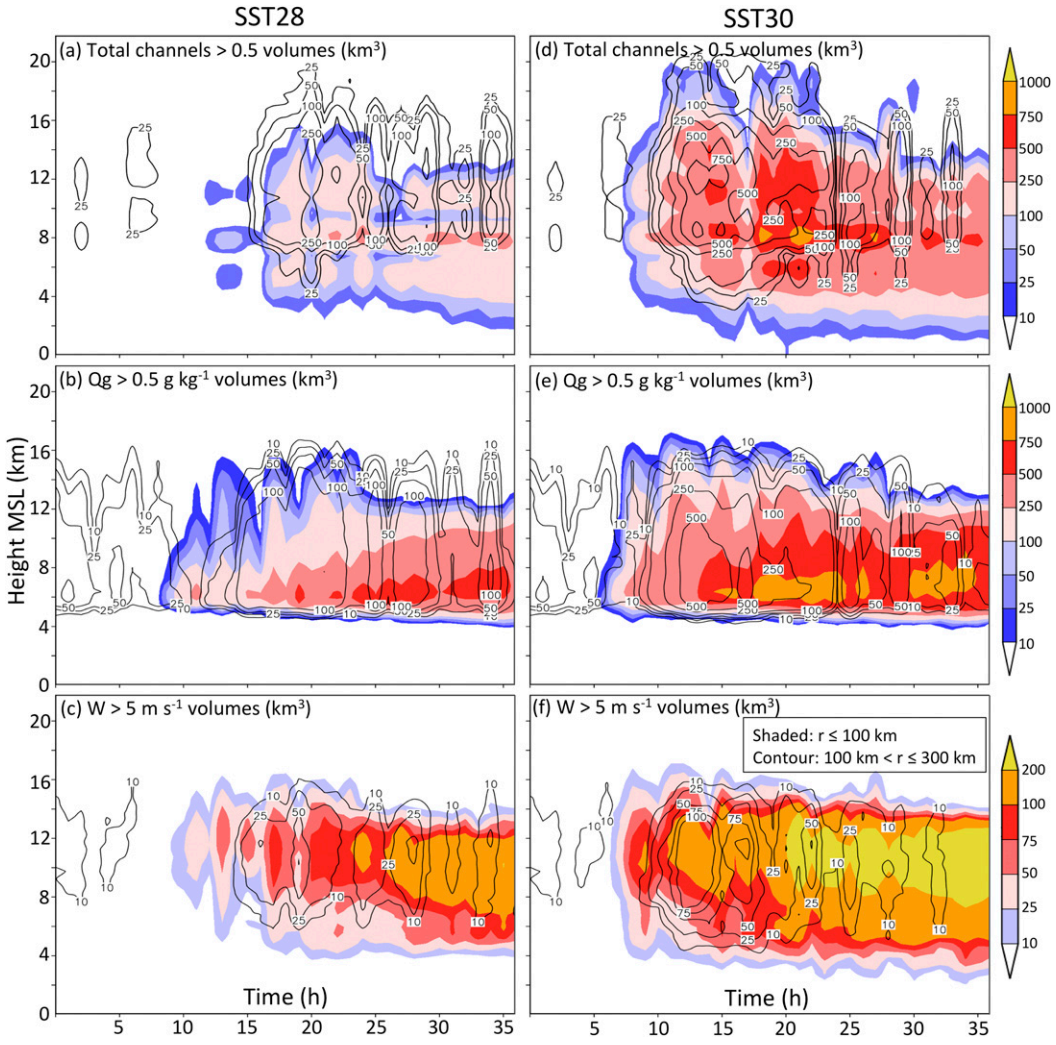

FIG. 5. Time–height volume plots (km^3) for SST28 of (a) total lightning channel (>0.5), (b) graupel (Qg > 0.5 g kg^{-1}), and (c) vertical velocity ($W > 5$ m s^{-1}). (d)–(f) As in (a)–(c), respectively, but for SST30. All time–height volume plots herein were computed from model data interpolated on a storm-centered cylindrical grid to better isolate the inner-core region (cylinder of radius $r = 100$ km) and outer region (cylinder volume within $100 < r \leq 300$ km), respectively. As in FM17, the volumes for a given variable A interpolated on the cylindrical grid are computed using the following procedures: At each level in the model, an algorithm counts instances when A exceeds a fixed threshold (e.g., 0.5 g kg^{-1} for graupel mass). The total count at each level is then scaled (multiplied) by the average volume of the grid cell (because of the stretched grid). Shaded areas show the volumes for the eyewall, and similarly, the contours show the volumes for the outer region. The legends for colors and shading are shown to the right of each row. To facilitate comparison, the contour levels are the same as for the shading.

electric potential, which inhibits channel propagation down to ground.

Overall, the convection in the outer region exhibited more vertically erect updrafts that reached higher altitudes compared to the inner core (cf. Fig. 6b and the left cell in Fig. 6d). As a result, graupel mass mixing ratio contours, 30-dBZ echo tops, and contours of cloud water contents within some of the strongest cells reached higher levels as well (cf. Fig. 6a and the left cell in Fig. 6b). The presence of graupel mass farther aloft in some of these cells coincides, in turn, with the bulk of the noninductive collisional charging occurring at higher levels as well, which is generally above the −10°C isotherm between 7 and 11 km (Figs. 6c,d). At these lower temperatures (i.e., ≤−10°C), graupel is charging more negatively, resulting in the positively charged ice crystals being lofted to upper levels above −30°C (~10 km). The updraft within the southern (left) cell of the outer region (Figs. 6b,d) reached ~15 m s^{-1}, causing both the negatively charged graupel at midlevels and positively

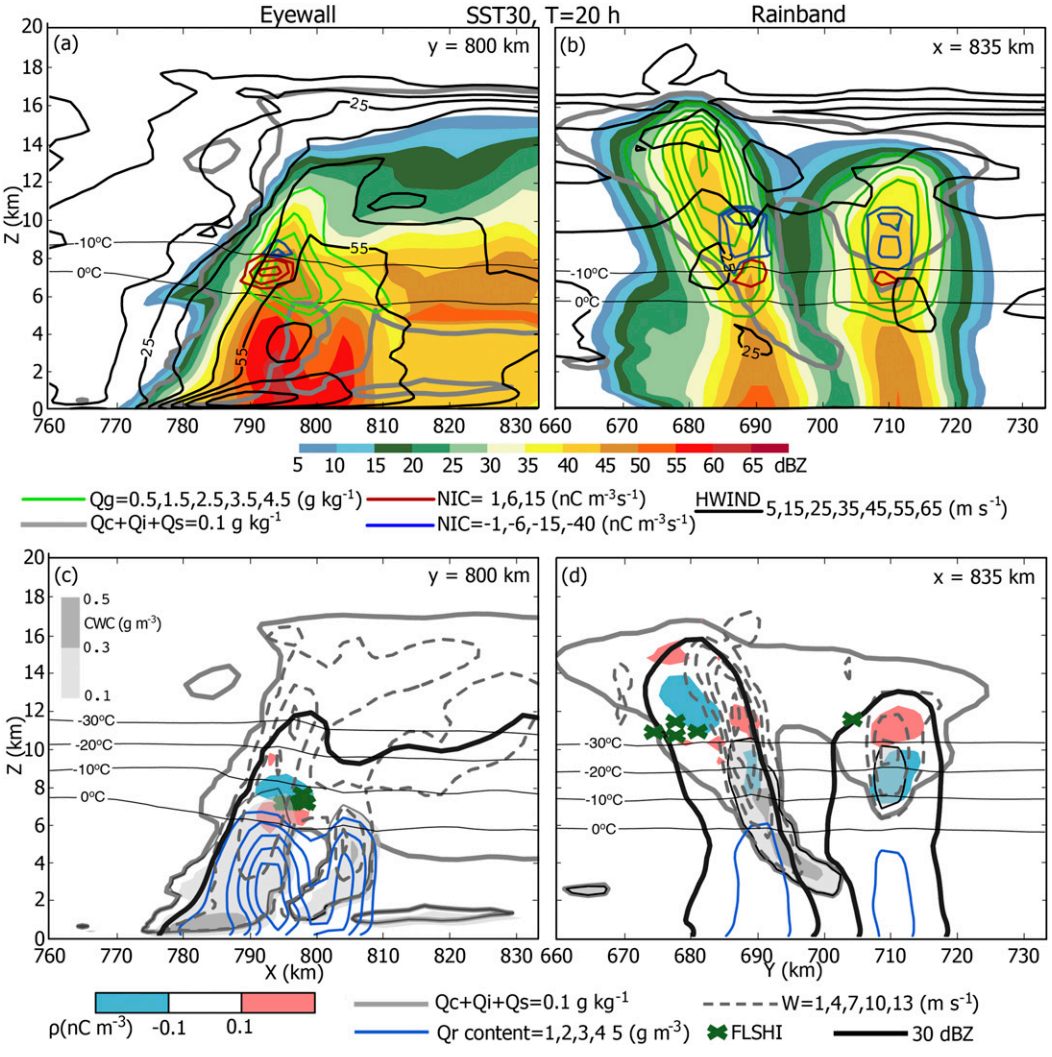

FIG. 6. Horizontal cross sections of selected electrical and microphysical variables for SST30 at 20 h across a representative section of convection in (a),(c) the eyewall (x–z plane) and (b),(d) the outer region (y–z plane). (a),(b) Radar reflectivity fields in their usual shading overlaid with graupel mass mixing ratio (Qg; g kg^{-1}; green contours), horizontal wind speed (HWIND; m s^{-1}; black contours), total positive (negative) noninductive charging rate (NIC; nC m^{-3} s^{-1}) in red (blue) contours, and the 0°C isotherm (thin horizontal black line). (c), (d) Positive (negative) net charge density ρ (nC m^{-3}) in red (blue) shading; CWC (g m^{-3}; gray shading); vertical velocity W (m s^{-1}; dashed gray contours); 30-dBZ echo outline (black contour); hourly flash initiation locations (FLSHI; green crosses); 0°, −10°, −20°, and −30°C isotherms (thin horizontal black line); and rainwater content (Qr; g m^{-3}; blue contours). The cloud outline, depicted by the 0.1 g kg^{-1} contour of the sum of cloud mixing ratio (Qc), ice mixing ratio (Qi), and snow mixing ratio (Qs), is also shown in all panels for reference. Legends for CWC are shown in (c). Legends for colors and shadings are indicated beneath each respective set of panels with all the contour levels explicitly listed for convenience.

charged ice crystals to be lofted to even higher levels above the −30°C isotherm (between 12 and 14 km). Also evident is a stark contrast in the rain mass content between the inner core and outer region (Figs. 6b,d and 2), which indicates a notably more aggressive warm rain regime in the inner core (FM17). This is also deduced from the 0.1 g m^{-3} cloud water content contours in the inner core that are largely confined below the −10°C isotherm (Fig. 6c), which indicates efficient autoconversion and accretion by rain. Those results, overall, are consistent with the control run in FM17.

b. *Analysis of proxy variables for lightning*

Complementing the volume plots described above, hourly time series of integrated inner-core and outer-region totals of various microphysical and kinematic

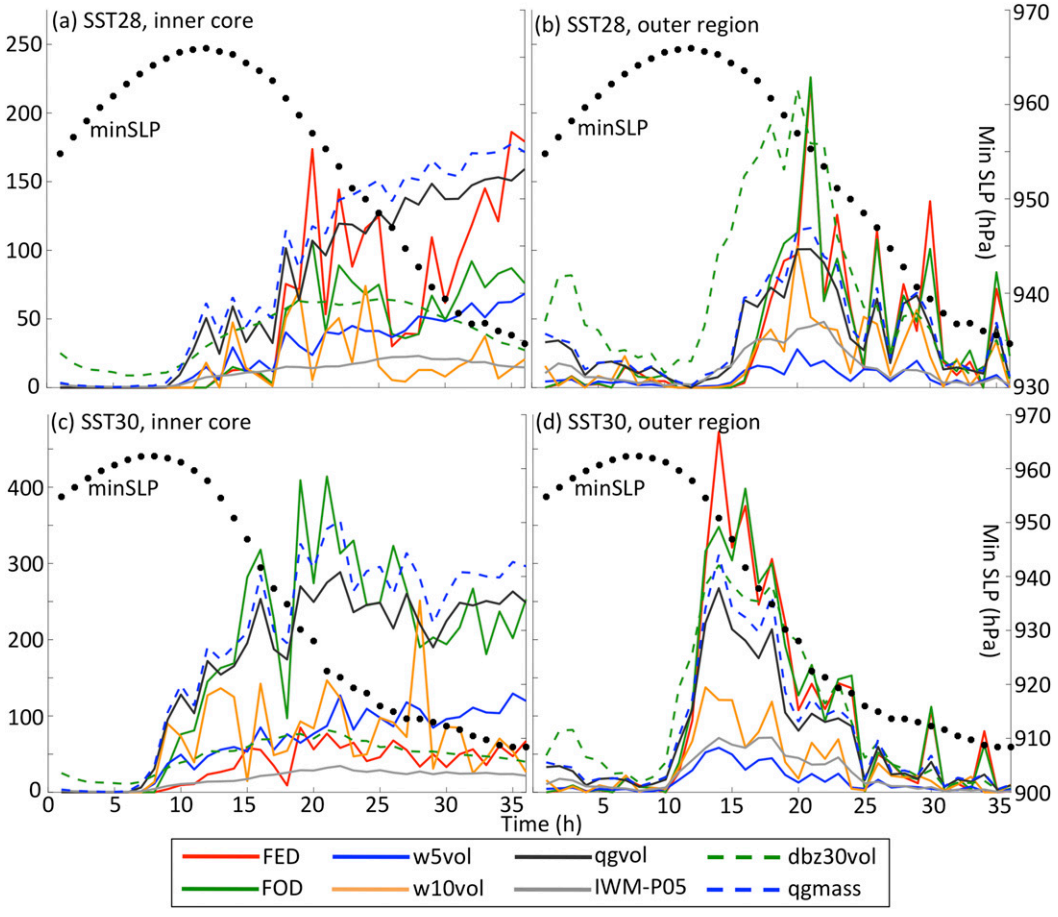

FIG. 7. Time series of hourly minSLP (hPa; right *y* axes; black dots) overlaid with the hourly time series (left *y* axes) of the following scaled quantities: FED (red), FOD (green), w5vol (blue), w10vol (orange), qgvol (black), IWM-P05 (dark gray), dbz30vol (dashed green), and qgmass (dashed blue). For convenience, the legend is illustrated at the bottom of the figure. The time series for SST28 are shown for (a) the inner core and (b) the outer region. (c),(d) As in (a) and (b), respectively, but for SST30. With the exception of minSLP, the variables listed in the legends in (a) were scaled by a factor ranging between 10^{-3} and 1 to fit on the *y* axis (Table 1). Note that the scale factors may differ between panels to improve visual comparisons. Further rationale for not placing emphasis on the scale factors includes (i) the trends rather than the absolute values are emphasized and (ii) these intend to complement the correlation statistics shown in Figs. 8 and 9 (which are invariant to scaling).

quantities known to be well associated with lightning in thunderstorms (referred to as proxy variables) are shown in Fig. 7 along with the pressure trace. The proxy variables examined in this study are total 5 m s^{-1} updraft volume (w5vol), total 10 m s^{-1} updraft volume (w10vol), total graupel echo volume (qgvol; threshold of 0.5 g kg^{-1}), total ice water mass (IWM), ice water mass computed using the ice water path defined as in Petersen et al. (2005; IWM-P05), 30-dBZ echo volume above 0°C (dbz30vol), and total graupel mass (qgmass). Because the trends rather than the absolute values are emphasized, these quantities were scaled in Fig. 7 to fit within the specified range of the *y* axis (Table 1). Given that the vast majority of these proxy variables for lightning still are, at best, very challenging to observe within TCs, it is desirable to establish quantitative estimates of their association with TC intensity change and total lightning. Taken together, these provide an overview of the association between intensity, microphysics, dynamics, and electrification with the TC. Furthermore, the Pearson correlation coefficient used in the subsequent statistical analyses is invariant to location and scale transformations. For clarity and brevity, only the most significant results are shown and discussed.

Three lightning metrics were evaluated in this analysis, namely, the integrated flash origin density (FOD), the integrated flash extent density (FED), and total lightning channels (or source) density. The FOD is a measure of the total lightning flash rate, FED provides additional information regarding the horizontal area of

TABLE 1. Units and scale factors accompanying the time series in Fig. 7 for the inner core and outer region in SST28 and SST30.

Lightning proxy variables	SST28		SST30	
	Inner core	Outer region	Inner core	Outer region
Integrated FED (h^{-1})	10^{-1}	10^{-1}	10^{-2}	10^{-1}
Integrated FOD (h^{-1})	1	1	1	1
w5vol (km^{-3} per average level)	10^{-2}	10^{-2}	10^{-2}	10^{-2}
w10vol (km^{-3} per average level)	10^{-1}	10^{-1}	10^{-1}	10^{-1}
qgvol (km^{-3} per average level)	10^{-2}	10^{-2}	10^{-2}	10^{-2}
IWM-P05 (kg)	10^{-2}	10^{-2}	10^{-3}	10^{-2}
dbz30vol (km^{-3} per average level)	10^{-2}	10^{-2}	10^{-3}	10^{-2}
qgmass (kg)	10^{-2}	10^{-2}	10^{-2}	10^{-2}

each flash, and the channel density is a measure of the integrated volumetric electrical activity. Although a single bidirectional lightning flash can traverse the same column multiple times, FED only counts one crossing per flash, while the total channel or source density rates sums them all (regardless of channel polarity). The analysis will focus on the (hourly integrated) FEDs, in part because the linear correlations between FOD, FED, and the sources densities were relatively high ($R >$ 0.95; not shown) but also because FED is perhaps the closest proxy for the lightning data delivered by the Geostationary Lightning Mapper (GLM) instrument (Goodman et al. 2013) aboard the Geostationary Operational Environmental Satellite R series (GOES-R; Gurka et al. 2006). Note also that because the pressure trace is chiefly dominated by an intensification signal (Fig. 1), these will be used interchangeably throughout the remainder of the analysis.

In line with the general trends obtained with the volumes at nearly all levels (Fig. 5), the respective totals of FOD and FED and most of the proxy variables in either the inner core or outer region (Fig. 7) follow a generally consistent evolution: for the inner core, the proxy variables show a notable increase after the onset of intensification in both simulations (Figs. 7a,c). In other words, marked increases in inner-core integrated FED and, therefore, lightning proxies indicate an ongoing intensification. It is interesting to note that, while nearly all the lightning proxy variables show a gradual increase in the inner core in SST28 throughout the simulation (Fig. 7a), this result does not hold for the inner core of SST30 wherein most proxy variables exhibit weak, if any, trends after about 22–23 h (Fig. 7c). This is because SST30 reaches its steady-state peak intensity status (and slower SLP decrease) more quickly than SST28, as evidenced by their respective pressure traces (Fig. 1). For the outer region, both simulations exhibit similar evolution, with all proxy variables increasing notably a few hours after the onset of intensification followed by a more gradual decrease after the period of most intense pressure drop, which again is more marked in SST30. This is because the areal coverage of the convection in the outer region decreases, which may be related to large-scale, midlevel subsidence induced by the TC secondary circulation in the far field (D. Nolan 2016, personal communications).

c. *Correlation statistics*

While not directly proving causation, predictors (i.e., proxy variables for lightning) can be useful if correlations are robust between a quantity that is more easily observed than a desired one that is not. Because of the relatively small sample size of the time series in Fig. 7 (i.e., 37 elements) and the desire to establish the statistical significance of the correlations obtained, the data were subjected to a bootstrapping technique (i.e., no a priori distribution assumed) involving 1000 random samples. Additional tests (not shown) were conducted using 5000 samples and revealed, overall, quantitatively similar results. To better visualize and interpret the results from the bootstrapped correlation statistics, box-and-whisker diagrams highlighting the significance at the 5% variance level are indicated in all the corresponding/appropriate diagrams, namely, Figs. 8–11. A given correlation is deemed insignificant whenever the 5% variance level crosses the zero-correlation line. For clarity, references to correlations in this section imply median correlation values, which also are displayed in Figs. 8–11. To further establish the robustness of the correlation statistics, one of the simulations (SST30) was restarted prior to the intensification of the TC and the model output data saved every 5 min for a 10-h period. The correlation statistics of this section were reevaluated with these data and revealed, overall, very similar qualitative behavior. Because the analysis based on the hourly output covers the entire duration of the simulation, and because hourly intervals remain more realistic in the context of systematic routine TC monitoring, the results obtained with the hourly dataset are shown.

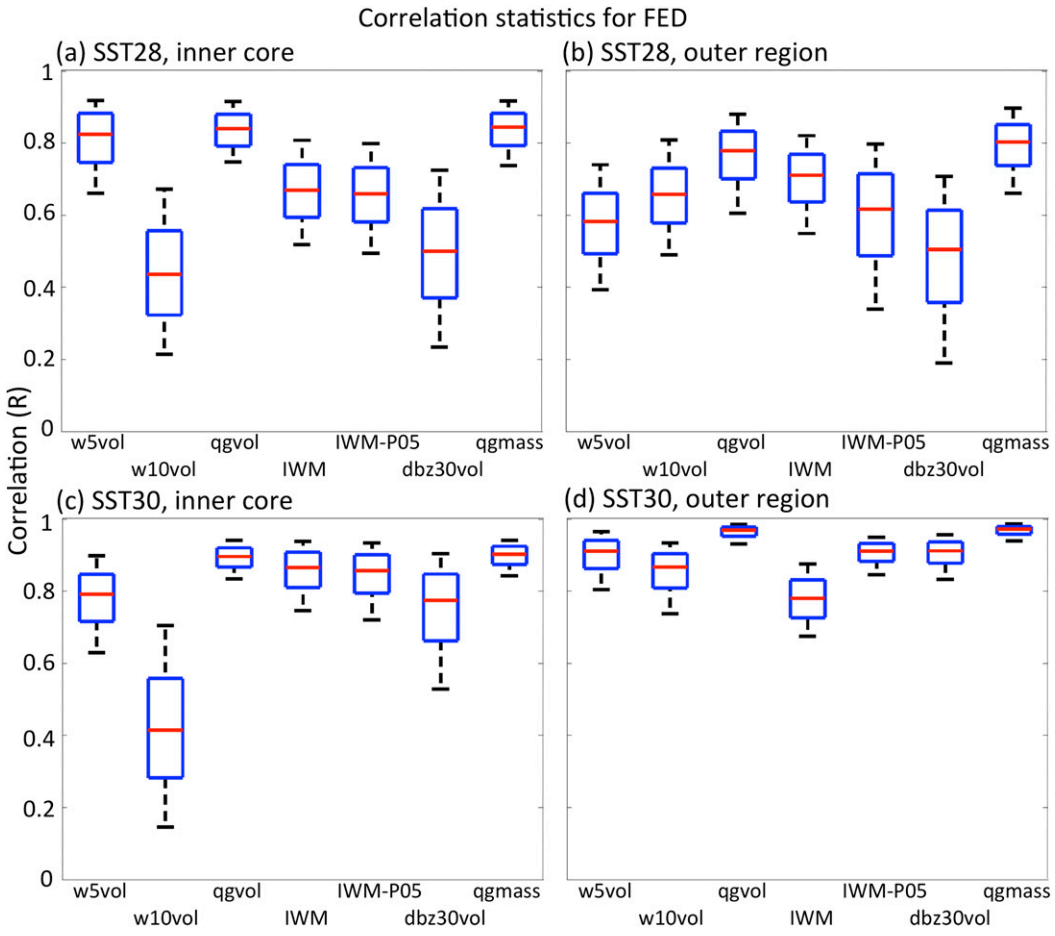

FIG. 8. Box-and-whisker plots of 1000-sample bootstrapped Pearson's correlations between the time series of hourly FED and the proxy variables listed on the x axis (and defined in the captions of Fig. 7). The red line depicts the median correlation. The blue box shows the lower and upper quartile (25% and 75%). The 2.5nd- and 97.5th-percentile correlation values are shown at the end bars of the dotted lines outside the blue box. Correlation statistics for SST28 are shown for (a) the inner core and (b) the outer region. (c),(d) As in (a) and (b), respectively, but for SST30. Given the very high correlation between FOD and FED (i.e., $R > 0.95$), the same bootstrapped correlation statistics for FOD are very similar and, thus, not shown. FED were preferred because this lightning metric is a better proxy for the anticipated data from GLM.

In both the inner core and outer regions and for each simulation, qgvol and qgmass produced the largest correlations with hourly integrated FED ($R \geq \sim 0.8$; Fig. 8). For the inner core, the smallest positive correlations were seen for w10vol and dbz30vol. The volumes of $10\,\mathrm{m\,s^{-1}}$ updrafts in the inner core in both simulations were substantially smaller (by about a factor of 4–5; not shown) than the $5\,\mathrm{m\,s^{-1}}$ volumes. Thus, the generally poor ($R < 0.5$) association obtained between FED and w10vol in the inner core can likely be explained by vertical velocities seldom reaching this threshold (i.e., $10\,\mathrm{m\,s^{-1}}$) in contrast to the outer region (Fig. 6), a result consistent with observations in mature TCs (Black and Hallett 1999).

In the outer region, most of the SST28 mean correlation values are <0.8, whereas all but one of the SST30 are >0.8. The time series in Figs. 7b and 7d give a similar qualitative impression, with the lightning in SST28 being more episodic (noisy) although still clearly correlated with qgmass. Overall, the outer region of SST30 produced collectively the highest correlations between FED rates and the proxy variables considered. Because these proxy variables were shown to be well associated with lightning in both continental and maritime thunderstorms, the systematic high correlations between FED and qgvol (or qgmass) indicate that the convection in both regions of both TCs collectively behaves similarly, consistent with Fig. 6 and Petersen et al. (2005).

Of interest to operational forecasters is the existence of potential relationships between lightning rates, lightning proxies such as the ones examined in Figs. 7 and 8, and

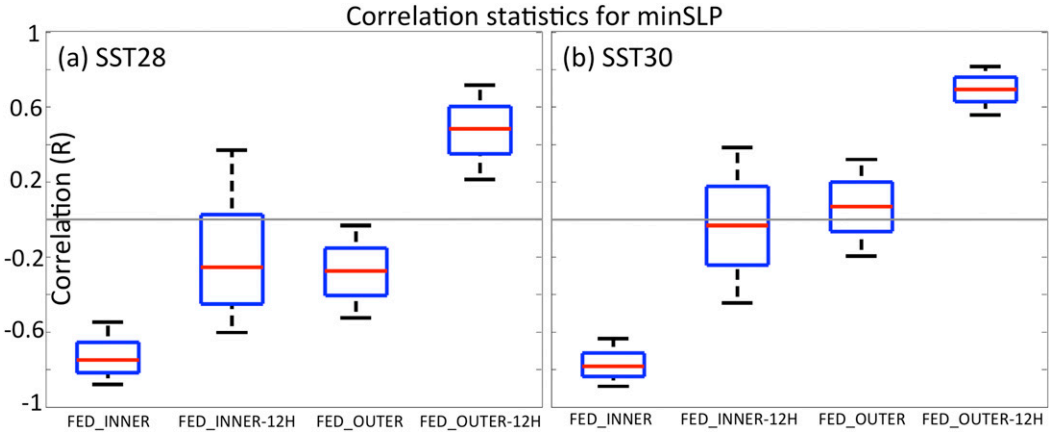

FIG. 9. As in Fig. 8, but between the hourly time series of minSLP and FED in the inner core and outer region for (a) SST28 and (b) SST30. Correlation statistics of minSLP with FEDs lagged by −12 h are also shown. As mentioned in Fig. 8, the statistics using FODs are very similar given the high correlation between FOD and FED ($R > 0.95$).

intensity trends. For instance, the predictors for the rapid intensification index (RII; DeMaria et al. 2012), which is a component of the Statistical Hurricane Intensity Prediction Scheme (SHIPS; Kaplan et al. 2010), make use of environmental parameters (input variables) such as ocean heat content or deep-layer shear. Recently, an experimental version of RII added the axisymmetric component of CG flash rates within the inner core and outer region of the TC derived from ground-based very low-frequency sensors (e.g., World Wide Lightning Location Network; Abarca et al. 2011; DeMaria et al. 2012).

A first step is to determine to what extent the simulated total lightning rates (as measured by the integrated FED) relate to the simulated pressure trends. Figure 9 shows that, for both simulations, the FED in the inner core is negatively correlated with the pressure trace ($R < -0.7$; i.e., that FED increases as minSLP decreases). The FED in the outer region shows overall statistically insignificant correlations as indicated by the 5% variance level remaining near or crossing the zero-correlation line (Fig. 9). The inner-core lightning has a longer, more gradual increase than the outer region (Fig. 7), which in contrast has a sharper rise followed by a longer decrease. Thus, when the FED time series in the outer region are shifted backward by 12 h, notably larger (and positive) R values are obtained ($R \sim 0.5$ for SST28 and $R \sim 0.7$ for SST30; Fig. 9). This indicates that the −12-h shift is capturing an association between the decrease in minSLP and the decrease in FED in the outer region. In other words, the initial decrease in minSLP leads the onset of the decrease in FED in the outer region by roughly 12 h. The increase in inner-core lightning is aligned with an ongoing or, even, the near end of a pressure fall, which is consistent with DeMaria et al. (2012). The lag seen for the outer-region lightning, however, contrasts with their findings.

This SLP-FED correlation result for the outer region may be dependent on the idealized setup, which cannot replicate the many complex mesoscale inhomogeneities existing in nature in the far-field environment of many TCs, and which could lead to increased lightning activity in the TC's outer region. Examples of such mesoscale features include regions of enhanced or reduced mid-tropospheric moisture content, regions of stronger or weak deep-layer shear, areas of higher or lower SSTs (e.g., loop currents), fronts/troughs, and jets (among others). Nevertheless, case studies with full mesoscale environmental initiation (Fierro and Reisner 2011; Fierro et al. 2015) have also seen simulated outer rainbands that are weaker (at least electrically) than observed, so this is a topic that merits further study.

When examining the correlation statistics for both simulations between the pressure trace and the lightning proxies first shown in Figs. 7 and 8, it is found that for the inner-core w5vol, qgvol, IWM, IWM-P05, and qgmass produce relatively high negative correlations ($R < -0.8$) with minSLP (Figs. 10a,c). These statistically significant high negative correlations can be inferred from their respective time series shown in Fig. 7a, wherein these lightning proxies increase markedly during the sharpest decrease in minSLP. The dbz30vol shows an overall moderate negative association with minSLP ($-0.6 < R < -0.4$) and w10vol only weak inner-core linkage. As indicated earlier, this lack of association between minSLP and w10vol in the inner core is chiefly explained by updraft speeds seldom reaching 10 m s^{-1} (example in

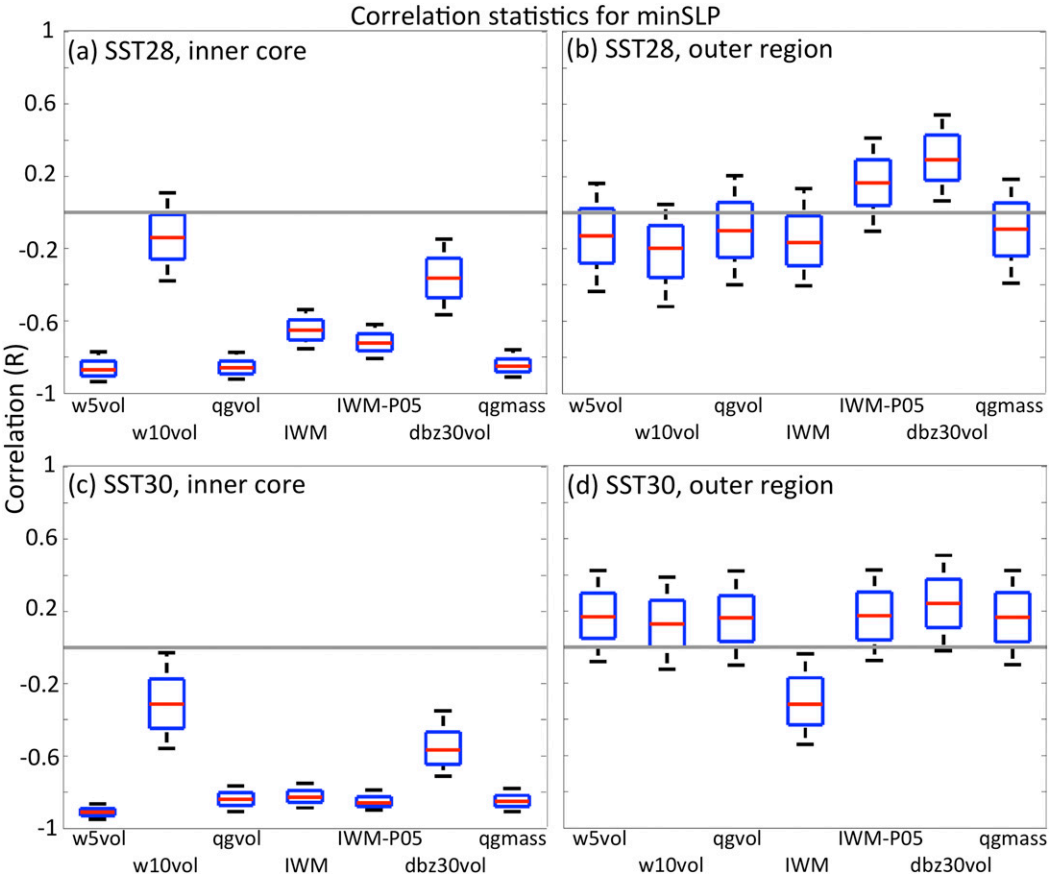

FIG. 10. As in Fig. 8, but for the correlation statistics with the hourly pressure trace (SLP; hPa).

Fig. 6b). These results for the inner core contrast with the outer region, where weak associations are found with the pressure trace (Figs. 10b,d).

When the time series of the lightning proxies of Fig. 10 are shifted backward by 12 h, the new correlation statistics exhibit dramatically contrasting results: namely, all the lightning proxy variables exhibit statistically significant high *positive* correlations ($0.6 < R < 0.9$) in the *outer region* (Figs. 11b,d). In the inner core, only dbz30vol is characterized by comparably high (positive) correlations ($R > 0.8$), with nearly all the other variables showing overall statistically insignificant linkages (the exception being w5vol for SST30 in Figs. 11a and 11c). In line with the correlation statistics obtained earlier between the hourly time series of FED and minSLP, Fig. 11 highlights that the salient trends in proxy variables in the outer region lag the trends in the pressure trace (i.e., deepening) by 12 h. Figure 7 further indicates that when most of these proxies experience a sharp increase in the inner core, the TC is already intensifying.

The above analysis focusing on Figs. 5–11 provided an overview of the relationships between the time series of lightning rates (FEDs), key lightning proxy variables, and minimum surface pressure trends (largely dominated by an intensification signal). A further analysis will now examine potential linear relationship(s) between data pairs composed of hourly lightning rates (FEDs) and each of the lightning proxy variables analyzed herein without considering their dependence in time. To achieve this, scatterplots of the paired data were constructed for the inner core and the outer region (Fig. 12). The datasets from both simulations were merged to broaden the range of each variable and, simultaneously, to increase the size of the sample to establish more general linear relationships.

Similar to the bootstrapped correlation statistics discussed earlier based on Fig. 8, the best linear fits with FED in the inner core and outer region are obtained with qgvol and qgmass with coefficient of determination R^2 exceeding 0.75 (Figs. 12b,c). The least significant relationships for both regions of the TC are obtained with dbz30vol and w10vol (Figs. 12a,e). Note that, overall, the integrated FED in the inner core exhibits good associations with all the proxy variables with $R^2 > 0.65$. In contrast, the FED in the outer region showed markedly

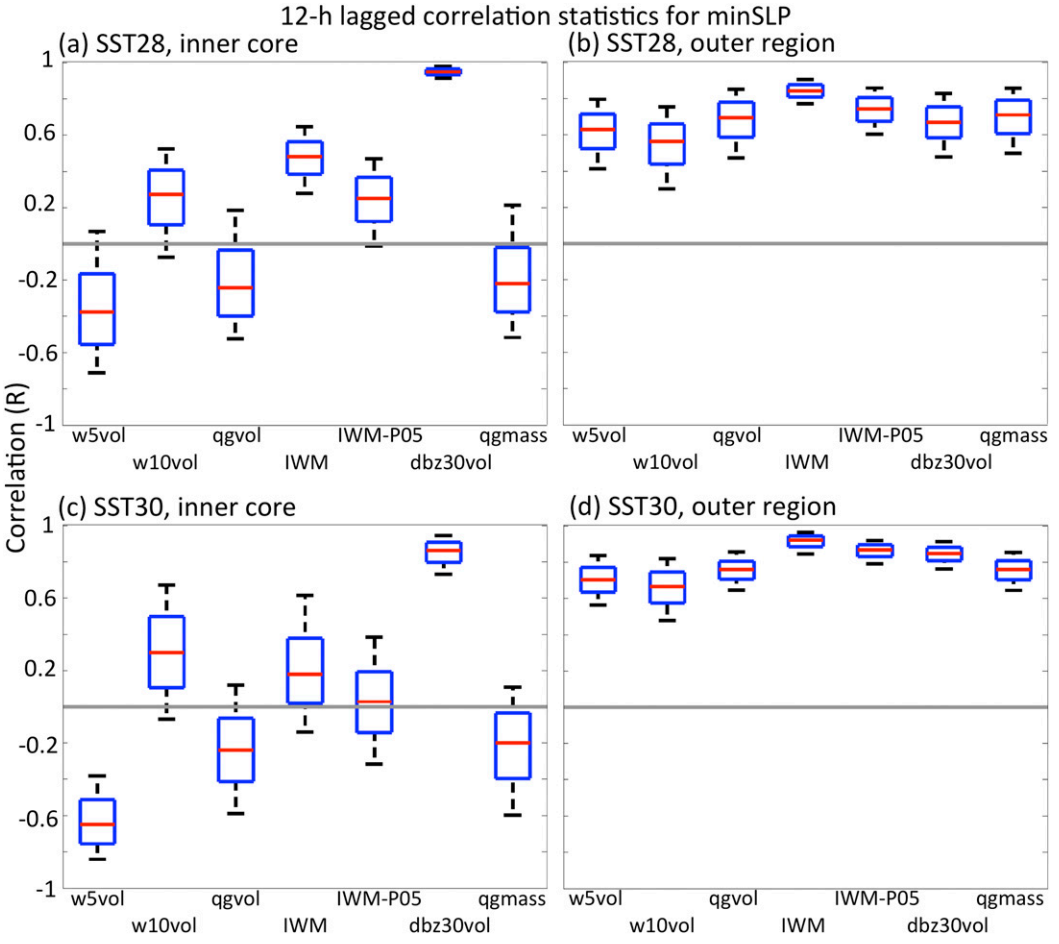

FIG. 11. As in Fig. 10, but with the time series of the proxy variables lagged by −12 h.

weaker relationships with dbz30vol (R^2 = 0.36; Fig. 12e), w10vol (R^2 = 0.35; Fig. 12a), and, arguably, showed a moderate association with both measures of ice water mass (R^2 = 0.59 for IWM-P05; Fig. 12f; not shown for IWM).

4. Conclusions and discussion

Using an explicit cloud-scale lightning model, this work used two TC simulations to investigate the relationships between intensification, lightning rates, and variables known to be well associated with lightning in thunderstorms over continent and the tropics. Given the recent successful launch of GOES-R, this study places emphasis on flash extent densities (FEDs) as this measure of lightning rate and area is a reasonable proxy for the data delivered by GLM.

As the TC intensified in both simulations, lightning rates in both the inner core ($r \leq 100$ km) and the outer region (100 km $< r \leq$ 300 km) experienced a notable increase as well, which coincided with an increase in updraft and graupel volumes in both regions. This result is consistent with the companion study of Fierro and Mansell (2017) and previous modeling studies of electrification within TCs (e.g., Fierro et al. 2015). Lightning in the outer region increased rapidly (3–5 h) just following the beginning of the minimum SLP decrease and then tended to slowly decrease during the continued rapid pressure fall. In contrast, lightning activity in the inner core remained relatively steady.

Bootstrapped correlation statistics using 1000 random samples revealed that an increase in lightning in the inner core indicated an ongoing pressure fall, consistent with DeMaria et al. (2012). When the lightning (FED) time series were shifted backward by 12 h, it was found that, in contrast to the inner core, the FED rates in the outer region exhibited statistically significant high positive correlations with the pressure trace. These correlations thus pick up both the gradual decreasing (15–20 h) and the sudden rapid increase (about 5 h) in the lightning trend.

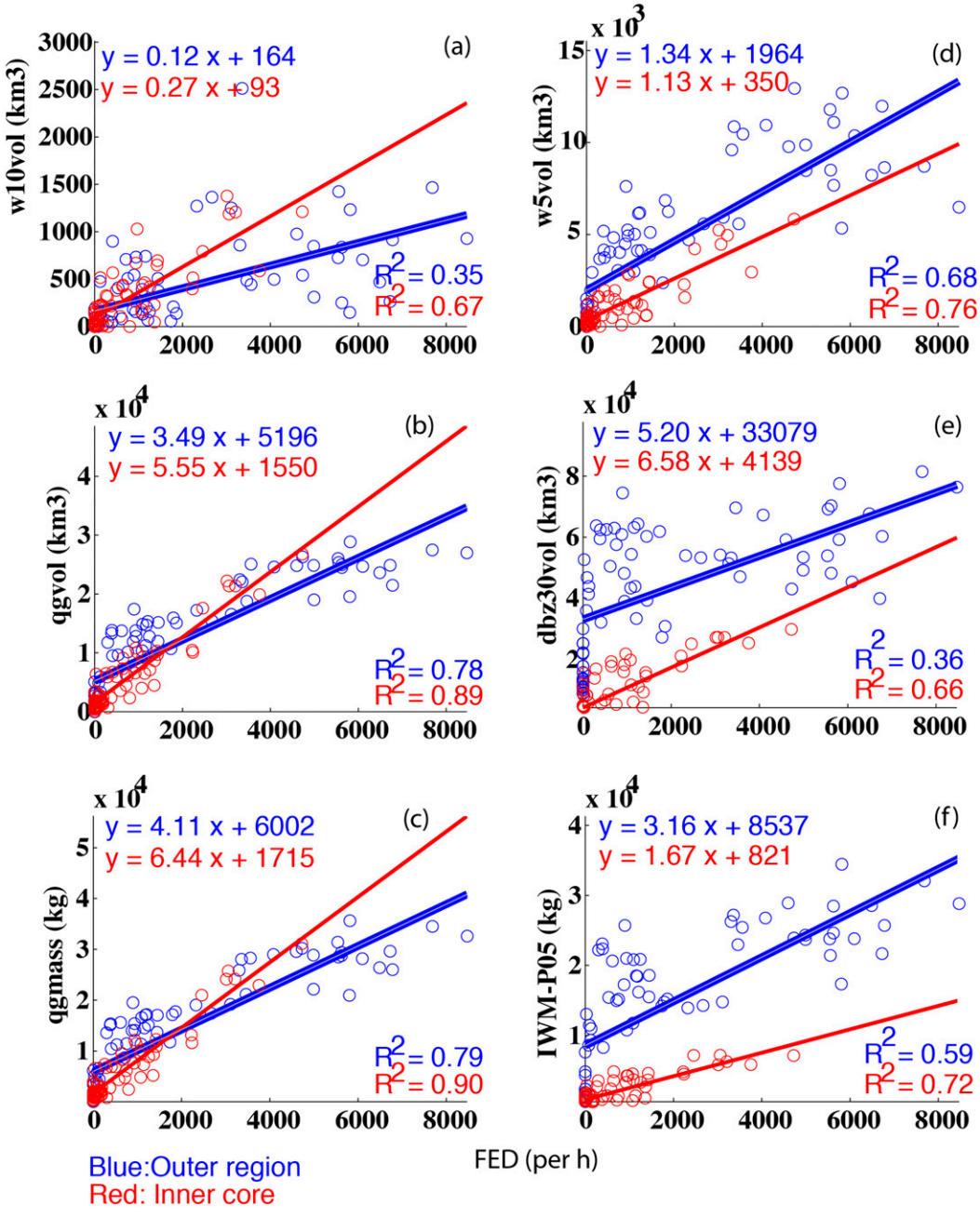

FIG. 12. Scatterplots between the hourly FED (x axis) and selected proxy variables on the y axis (defined in Fig. 7) for the inner core (red) and the outer region (blue). To broaden the range of FED rates and data points, these graphs were constructed using the output from both SST28 and SST30. The coefficients of determination (or R^2 values) for the linear best-fit equations shown on the top left of each panel also are indicated at the bottom right of each corresponding panel. All results are statistically significant at the $p = 0.01$ level.

Although DeMaria et al. (2012) primarily used CG data, this contrasts with their main results that the outer region was a better surrogate/predictor for TC intensification.

During the period of most intense pressure drop, nearly all the lightning proxies examined herein—namely, the 5 and 10 $\mathrm{m\,s^{-1}}$ updraft volumes, 30-dBZ echo volume above 0°C, two definitions of ice water path, graupel volume, and graupel mass—increased in both the inner core and outer region. The bootstrapped correlation statistics revealed that the increase of most of the lightning proxy variables in the inner core was negatively correlated with the pressure trace. When the time series

of these proxies in the outer region were lagged by −12 h, it was found that, akin to the FEDs, these variables became more positively correlated with the pressure trace. In other words, the decrease in these variables in the outer region of the TC lags the pressure trends by about 12 h.

One notable caveat of the present simulations is that the lightning and deep moist convection in the outer region progressively wane in both simulations. This was traced back to a gradual reduction of midlevel relative humidity potentially associated with the development of large-scale subsidence in the far field (D. Nolan 2016, personal communications). Similar rainband evolution has been well documented for long integrations of idealized TCs. Additional idealized simulations performed either with COMMAS or with the Weather Research and Forecasting (WRF) Model on noticeably larger domains (2–6 times the size in kilometers) with similar and different physics exhibited similar behavior in the outer region, as did simulations that included an additional nudging term for q_v that gradually forced the simulated q_v back toward its initial larger value. It is not clear whether outer-region convection can be improved through the use of more sophisticated physics (e.g., coupled air–sea ocean model, full radiation scheme) or if perhaps interactions with environmental inhomogeneities play a more important role, although case studies with real-data initialization (Fierro and Reisner 2011; Fierro et al. 2015) have also exhibited outer rainbands that were electrically weaker than observed.

The second limitation worth underlining is that while the model was able to reasonably reproduce the increase in inner-core lightning *during* intensification documented in DeMaria et al. (2012), the results for the outer region were inconsistent with their study. This is because in contrast to inner-core lightning, the invigoration of convection in the far field of the TC also owes its existence to mesoscale inhomogeneities—such as SST gradients, midtropospheric moisture content gradients, fronts/jets—that the current idealized setup does not include. Another issue is that there is virtually no lightning before the intensification in these simulations, and thus, they may not represent the mean of cases considered by DeMaria et al. (2012).

Consequently, future modeling endeavors wishing to examine the possibly more complex relationships between pressure fall and rainband lightning should make use of an explicit cloud-scale model able to simulate real case studies through inhomogeneous initializations via reanalysis or forecast data (e.g., Fierro et al. 2015). Data assimilation could also be considered to further improve the shorter-term representation of the convective structure of the TC (e.g., Fierro and Reisner 2011; Fierro et al. 2015).

Acknowledgments. Funding was provided by NOAA/Office of Oceanic and Atmospheric Research under NOAA–University of Oklahoma Cooperative Agreement NA11OAR4320072, U.S. Department of Commerce. This work was further supported by NOAA, U.S. Department of Commerce, under Grants NOAA-OAR-CIPO-2014-2003893 and NOAA-NWS-NWSPO-2016-2004610. The simulations were made possible through computing resources provided by NOAA (HPC "Jet") with auxiliary computing resources also provided by the Oklahoma Supercomputing Center for Education and Research (OSCER). The authors thank Mark DeMaria and John Knaff for their useful discussions that led to the elaboration of this work. Thanks also go out to Dave Jorgensen for providing insightful comments on an earlier version of this manuscript.

REFERENCES

Abarca, S. F., K. L. Corbosiero, and D. Vollaro, 2011: The World Wide Lightning Location Network and convective activity in tropical cyclones. *Mon. Wea. Rev.*, **139**, 175–191, https://doi.org/10.1175/2010MWR3383.1.

Anthes, R. A., 2003: Hot towers and hurricanes: Early observations, theories, and models. *Cloud Systems, Hurricanes, and the Tropical Rainfall Measuring Mission (TRMM)—A Tribute to Dr. Joanne Simpson*, *Meteor. Monogr.*, No. 40, Amer. Meteor. Soc., 139–148, https://doi.org/10.1175/0065-9401(2003)029<0139:CHTAHE>2.0.CO;2.

Black, R. A., and J. Hallett, 1999: Electrification of the hurricane. *J. Atmos. Sci.*, **56**, 2004–2028, https://doi.org/10.1175/1520-0469(1999)056<2004:EOTH>2.0.CO;2.

Boccippio, D. J., K. L. Cummins, H. J. Christian, and S. J. Goodman, 2001: Combined satellite- and surface-based estimation of the intracloud–cloud-to-ground lightning ratio over the continental United States. *Mon. Wea. Rev.*, **129**, 108–122, https://doi.org/10.1175/1520-0493(2001)129,0108:CSASBE.2.0.CO;2.

Bovalo, C., C. Barthe, N. Yu, and N. Bègue, 2014: Lightning activity within tropical cyclones in the south west Indian Ocean. *J. Geophys. Res. Atmos.*, **119**, 8231–8244, https://doi.org/10.1002/2014JD021651.

Brooks, I. M., C. P. R. Saunders, R. P. Mitzeva, and S. L. Peck, 1997: The effect on thunderstorm charging of the rate of rime accretion by graupel. *Atmos. Res.*, **43**, 277–295, https://doi.org/10.1016/S0169-8095(96)00043-9.

Cecil, D. J., and E. J. Zipser, 2002: Reflectivity, ice scattering, and lightning characteristics of hurricane eyewalls and rainbands. Part II: Intercomparison of observations. *Mon. Wea. Rev.*, **130**, 785–801, https://doi.org/10.1175/1520-0493(2002)130<0785:RISALC>2.0.CO;2.

——, ——, and S. W. Nesbitt, 2002: Reflectivity, ice scattering, and lightning characteristics of hurricane eyewalls and rainbands. Part I: Quantitative description. *Mon. Wea. Rev.*, **130**, 769–784, https://doi.org/10.1175/1520-0493(2002)130<0769:RISALC>2.0.CO;2.

Coniglio, M. C., D. J. Stensrud, and L. J. Wicker, 2006: Effects of upper-level shear on the structure and maintenance of strong quasi-linear mesoscale convective systems. *J. Atmos. Sci.*, **63**, 1231–1252, https://doi.org/10.1175/JAS3681.1.

DeMaria, M., R. T. DeMaria, J. A. Knaff, and D. Molenar, 2012: Tropical cyclone lightning and rapid intensity change. *Mon. Wea. Rev.*, **140**, 1828–1842, https://doi.org/10.1175/MWR-D-11-00236.1.

Dendy, J. E., Jr., 1987: Two multigrid methods for three-dimensional problems with discontinuous and anisotropic coefficients. *SIAM J. Sci. Stat. Comput.*, **8**, 673–685, https://doi.org/10.1137/0908059.

——, and J. D. Moulton, 2010: Black box multigrid with coarsening by a factor of three. *Numer. Linear Algebra Appl.*, **17**, 577–598, https://doi.org/10.1002/nla.705.

Fierro, A. O., and J. M. Reisner, 2011: High-resolution simulation of the electrification and lightning of Hurricane Rita during the period of rapid intensification. *J. Atmos. Sci.*, **68**, 477–494, https://doi.org/10.1175/2010JAS3659.1.

——, and E. R. Mansell, 2017: Electrification and lightning in idealized simulations of a hurricane-like vortex subject to wind shear and sea surface temperature cooling. *J. Atmos. Sci.*, **74**, 2023–2041, https://doi.org/10.1175/JAS-D-16-0270.1.

——, M. S. Gilmore, E. R. Mansell, L. J. Wicker, and J. M. Straka, 2006: Electrification and lightning in an idealized boundary-crossing supercell simulation of 2 June 1995. *Mon. Wea. Rev.*, **134**, 3149–3172, https://doi.org/10.1175/MWR3231.1.

——, L. M. Leslie, E. R. Mansell, J. M. Straka, D. R. MacGorman, and C. Ziegler, 2007: A high-resolution simulation of the microphysics and electrification in an idealized hurricane-like vortex. *Meteor. Atmos. Phys.*, **98**, 13–33, https://doi.org/10.1007/s00703-006-0237-0.

——, X.-M. Shao, J. M. Reisner, J. D. Harlin, and T. Hamlin, 2011: Evolution of eyewall convective events as indicated by intracloud and cloud-to-ground lightning activity during the rapid intensification of Hurricanes Rita and Katrina. *Mon. Wea. Rev.*, **139**, 1492–1504, https://doi.org/10.1175/2010MWR3532.1.

——, E. R. Mansell, C. Ziegler, and D. R. MacGorman, 2013: The implementation of an explicit charging and discharge lightning scheme within the WRF-ARW Model: Benchmark simulations with a continental squall line and a tropical cyclone. *Mon. Wea. Rev.*, **141**, 2390–2415, https://doi.org/10.1175/MWR-D-12-00278.1.

——, ——, D. R. MacGorman, and C. Ziegler, 2015: Explicitly simulated electrification and lightning within a tropical cyclone based on the environment of Hurricane Isaac (2012). *J. Atmos. Sci.*, **72**, 4167–4193, https://doi.org/10.1175/JAS-D-14-0374.1.

Goodman, S. J., and Coauthors, 2013: The GOES-R Geostationary Lightning Mapper (GLM). *Atmos. Res.*, **125–126**, 34–49, https://doi.org/10.1016/j.atmosres.2013.01.006.

Guimond, S. R., G. M. Heymsfield, and F. J. Turk, 2010: Multiscale observations of Hurricane Dennis (2005): The effects of hot towers on rapid intensification. *J. Atmos. Sci.*, **67**, 633–654, https://doi.org/10.1175/2009JAS3119.1.

——, ——, P. D. Reasor, and A. C. Didlake Jr., 2016: The rapid intensification of Hurricane Karl (2010): New remote sensing observations of convective bursts from the Global Hawk platform. *J. Atmos. Sci.*, **73**, 3617–3639, https://doi.org/10.1175/JAS-D-16-0026.1.

Gurka, J. J., T. A. Schmit, T. M. Renkevens, M. M. Gunshor, and J. Li, 2006: 2006 update on baseline instruments for GOES-R series. *Atmospheric and Environmental Remote Sensing Data Processing and Utilization II: Perspective on Calibration/Validation Initiatives and Strategies*, A. H. L. Huang and H. J. Bloom, Eds., Society of Photo-Optical Instrumentation Engineers (SPIE Proceedings, Vol. 6301), 63010H, https://doi.org/10.1117/12.683701.

Hazelton, A. T., R. E. Hart, and R. F. Rogers, 2017: Analyzing simulated convective bursts in two Atlantic hurricanes. Part II: Intensity change due to bursts. *Mon. Wea. Rev.*, **145**, 3095–3117, https://doi.org/10.1175/MWR-D-16-0268.1.

Hendricks, E. A., M. T. Montgomery, and C. A. Davis, 2004: The role of "vortical" hot towers in the formation of Tropical Cyclone Diana (1984). *J. Atmos. Sci.*, **61**, 1209–1232, https://doi.org/10.1175/1520-0469(2004)061<1209:TROVHT>2.0.CO;2.

Kaplan, J., M. DeMaria, and J. A. Knaff, 2010: A revised tropical cyclone rapid intensification index for the Atlantic and eastern North Pacific basins. *Wea. Forecasting*, **25**, 220–241, https://doi.org/10.1175/2009WAF2222280.1.

Kelley, O. A., J. Stout, and J. B. Halverson, 2004: Tall precipitation cells in tropical cyclone eyewalls are associated with tropical cyclone intensification. *Geophys. Res. Lett.*, **31**, L24112, https://doi.org/10.1029/2004GL021616.

Klemp, J. B., and R. B. Wilhelmson, 1978: The simulation of three-dimensional convective storm dynamics. *J. Atmos. Sci.*, **35**, 1070–1096, https://doi.org/10.1175/1520-0469(1978)035<1070:TSOTDC>2.0.CO;2.

Kuhlman, K. M., C. L. Ziegler, E. R. Mansell, D. R. MacGorman, and J. M. Straka, 2006: Numerically simulated electrification and lightning of the 29 June 2000 STEPS supercell storm. *Mon. Wea. Rev.*, **134**, 2734–2757, https://doi.org/10.1175/MWR3217.1.

Lang, T. J., and S. A. Rutledge, 2002: Relationships between convective storm kinematics, precipitation, and lightning. *Mon. Wea. Rev.*, **130**, 2492–2506, https://doi.org/10.1175/1520-0493(2002)130<2492:RBCSKP>2.0.CO;2.

Lyons, W. A., M. G. Venne, P. G. Black, and R. C. Gentry, 1989: Hurricane lightning: A new diagnostic tool for tropical storm forecasting? Preprints, *18th Conf. on Hurricanes and Tropical Meteorology*, San Diego, CA, Amer. Meteor. Soc., 113–114.

MacGorman, D. R., and W. D. Rust, 1998: *The Electrical Nature of Storms*. Oxford University Press, 422 pp.

——, D. W. Burgess, V. Mazur, W. D. Rust, W. L. Taylor, and B. C. Johnson, 1989: Lightning rates relative to tornadic storm evolution on 22 May 1981. *J. Atmos. Sci.*, **46**, 221–251, https://doi.org/10.1175/1520-0469(1989)046<0221:LRRTTS>2.0.CO;2.

Mansell, E. R., and C. L. Ziegler, 2013: Aerosol effects on simulated storm electrification and precipitation in a two-moment bulk microphysics model. *J. Atmos. Sci.*, **70**, 2032–2050, https://doi.org/10.1175/JAS-D-12-0264.1.

——, D. R. MacGorman, C. L. Ziegler, and J. M. Straka, 2002: Simulated three-dimensional branched lightning in a numerical thunderstorm model. *J. Geophys. Res.*, **107**, 4075, https://doi.org/10.1029/2000JD000244.

——, ——, ——, and ——, 2005: Charge structure and lightning sensitivity in a simulated multicell storm. *J. Geophys. Res.*, **110**, D12101, https://doi.org/10.1029/2004JD005287.

——, C. L. Ziegler, and C. Bruning, 2010: Simulated electrification of a small thunderstorm with two-moment bulk microphysics. *J. Atmos. Sci.*, **67**, 171–194, https://doi.org/10.1175/2009JAS2965.1.

Molinari, J., P. K. Moore, V. P. Idone, R. W. Henderson, and A. B. Saljoughy, 1994: Cloud-to-ground lightning in Hurricane Andrew. *J. Geophys. Res.*, **99**, 16 665–16 676, https://doi.org/10.1029/94JD00722.

——, ——, and ——, 1999: Convective structure of hurricanes as revealed by lightning locations. *Mon. Wea. Rev.*, **127**, 520–534, https://doi.org/10.1175/1520-0493(1999)127<0520:CSOHAR>2.0.CO;2.

Montgomery, M. T., M. E. Nicholls, T. A. Cram, and A. B. Saunders, 2006: A vortical hot tower route to tropical

cyclogenesis. *J. Atmos. Sci.*, **63**, 355–386, https://doi.org/10.1175/JAS3604.1.

Nolan, D. S., Y. Moon, and D. P. Stern, 2007: Tropical cyclone intensification from asymmetric convection: Energetics and efficiency. *J. Atmos. Sci.*, **64**, 3377–3405, https://doi.org/10.1175/JAS3988.1.

Petersen, W. A., J. Christian, and S. A. Rutledge, 2005: TRMM observations of the global relationship between ice water content and lightning. *Geophys. Res. Lett.*, **32**, L14819, https://doi.org/10.1029/2005GL023236.

Pielke, R. A., Jr., and C. W. Landsea, 1998: Normalized hurricane damages in the United States: 1925–1995. *Wea. Forecasting*, **13**, 621–631, https://doi.org/10.1175/1520-0434(1998)013<0621:NHDITU>2.0.CO;2.

Price, C., M. Asfur, and Y. Yair, 2009: Maximum hurricane intensity preceded by increase in lightning frequency. *Nat. Geosci.*, **2**, 329–332, https://doi.org/10.1038/ngeo477.

Rogers, R. F., P. Reasor, and S. Lorsolo, 2013: Airborne Doppler observations of the inner-core structural differences between intensifying and steady-state tropical cyclones. *Mon. Wea. Rev.*, **141**, 2970–2991, https://doi.org/10.1175/MWR-D-12-00357.1.

——, J. A. Zhang, J. Zawislak, G. R. Alvey, E. J. Zipser, and H. Jiang, 2016: Observations of the structure and evolution of Hurricane Edouard (2014) during intensity change. Part II: Kinematic structure and the distribution of deep convection. *Mon. Wea. Rev.*, **144**, 3355–3376, https://doi.org/10.1175/MWR-D-16-0017.1.

Rotunno, R., and K. A. Emanuel, 1987: An air–sea interaction theory for tropical cyclones. Part II: Evolutionary study using a nonhydrostatic axisymmetric numerical model. *J. Atmos. Sci.*, **44**, 542–561, https://doi.org/10.1175/1520-0469(1987)044<0542:AAITFT>2.0.CO;2.

Samsury, C. E., and R. E. Orville, 1994: Cloud-to-ground lightning in tropical cyclones: A study of Hurricanes Hugo (1989) and Jerry (1989). *Mon. Wea. Rev.*, **122**, 1887–1896, https://doi.org/10.1175/1520-0493(1994)122<1887:CTGLIT>2.0.CO;2.

Saunders, C. P. R., and L. S. Peck, 1998: Laboratory studies of the influence of the rime accretion rate on charge transfer during crystal/graupel collisions. *J. Geophys. Res.*, **103**, 13 949–13 956, https://doi.org/10.1029/97JD02644.

Schmidt, S., C. Kemfert, and P. Höppe, 2009: Tropical cyclone losses in the USA and the impact of climate change—A trend analysis based on data from a new approach to adjusting storm losses. *Environ. Impact Assess. Rev.*, **29**, 359–369, https://doi.org/10.1016/j.eiar.2009.03.003.

Schultz, C. J., W. A. Petersen, and L. D. Carey, 2011: Lightning and severe weather: A comparison between total and cloud-to-ground lightning trends. *Wea. Forecasting.*, **26**, 744–755, https://doi.org/10.1175/WAF-D-10-05026.1.

Shao, X. M., and Coauthors, 2005: Katrina and Rita were lit up with lightning. *Eos, Trans. Amer. Geophys. Union*, **86**, 398, https://doi.org/10.1029/2005EO420004.

Smith, R. K., and M. T. Montgomery, 2015: Toward clarity on understanding tropical cyclone intensification. *J. Atmos. Sci.*, **72**, 3020–3031, https://doi.org/10.1175/JAS-D-15-0017.1.

Squires, K., and S. Businger, 2008: The morphology of eyewall lightning outbreaks in two category 5 hurricanes. *Mon. Wea. Rev.*, **136**, 1706–1726, https://doi.org/10.1175/2007MWR2150.1.

Stevenson, S. N., K. L. Corbosiero, and S. F. Abarca, 2016: Lightning in eastern North Pacific tropical cyclones: A comparison to the North Atlantic. *Mon. Wea. Rev.*, **144**, 225–239, https://doi.org/10.1175/MWR-D-15-0276.1.

Thomas, J. N., N. Solorzano, S. A. Cummer, and R. H. Holzworth, 2010: Polarity and energetics of inner core lightning in three intense North Atlantic hurricanes. *J. Geophys. Res.*, **115**, A00E15, https://doi.org/10.1029/2009JA014777.

Wicker, L. J., and R. B. Wilhelmson, 1995: Simulation and analysis of tornado development and decay within a three-dimensional supercell thunderstorm. *J. Atmos. Sci.*, **52**, 2675–2703, https://doi.org/10.1175/1520-0469(1995)052<2675:SAAOTD>2.0.CO;2.

Wiens, K. C., S. A. Rutledge, and S. A. Tessendorf, 2005: The 29 June 2000 supercell observed during STEPS. Part II: Lightning and charge structure. *J. Atmos. Sci.*, **62**, 4151–4177, https://doi.org/10.1175/JAS3615.1.

Williams, E., and N. Renno, 1993: An analysis of the conditional instability of the tropical atmosphere. *Mon. Wea. Rev.*, **121**, 21–36, https://doi.org/10.1175/1520-0493(1993)121<0021:AAOTCI>2.0.CO;2.

Ziegler, C. L., 1985: Retrieval of thermal and microphysical variables in observed convective storms. Part I: Model development and preliminary testing. *J. Atmos. Sci.*, **42**, 1487–1509, https://doi.org/10.1175/1520-0469(1985)042<1487:ROTAMV>2.0.CO;2.

——, D. R. MacGorman, J. E. Dye, and P. S. Ray, 1991: A model evaluation of noninductive graupel-ice charging in the early electrification of a mountain thunderstorm. *J. Geophys. Res.*, **96**, 12 833–12 855, https://doi.org/10.1029/91JD01246.